EVALUATIONS OF TEMPERATURE MEASUREMENTS BY NEAR-INFRARED THERMOGRAPHY IN POWDER-BASED ELECTRON-BEAM ADDITIVE MANUFACTURING

Steven Price*, Ken Cooper**, Kevin Chou*

*Department of Mechanical Engineering
The University of Alabama, Tuscaloosa, AL 35487, USA

**Advanced Manufacturing Technology Team
Marshall Space Flight Center, Huntsville, AL 35812, USA
REVIEWED, Accepted August 16, 2012

Abstract

Powder-based electron beam additive manufacturing (EBAM) has gained increased usage in different industries. Process monitoring such as temperatures may offer important information. However, temperature measurements in EBAM are challenging because of high temperature ranges, extreme gradients and fast transient response.

In this study, temperature measurements during the EBAM process, in particular, around the electron beam scanning area, were attempted using a near-infrared thermal camera. The obtained temperature data demonstrated the feasibility of such a measuring technique. The thermal camera was able to capture the pre-heating, contour melting, and hatch melting events. Further, the achievable spatial resolution is around 12 μm when using a 350 mm lens.

Introduction

Additive manufacturing (AM) based on "layer-by-layer" fabrications is a fast-growing emerging technology, by which physical solid parts are made directly from electronic data, generally files from computer-aided design (CAD) software. This group of technologies offers many design and manufacturing advantages such as short lead time, part geometry complexity, and no tooling, etc. Electron Beam Additive Manufacturing (EBAM) is one of relatively new AM technologies. Similar to electron-beam welding, EBAM utilizes a high-energy electron beam to melt and fuse metal powders and build parts in an additive fashion. Moreover, EBAM is one of a few AM technologies capable of making full-density metallic parts and has drastically extended AM applications for direct digital manufacturing of structural components. There are two kinds of EBAM technologies, different in raw material stock: powder-bed vs. wire-feed. The latter one, developed by NASA's Langley Research Center, is known as electron beam freeform fabrications (EBF^3) in industry, and is mainly utilized for repair and adding common features to a large structure. On the other hand, the powder-based EBAM technology, commercialized by Arcam AB, has been explored for more net-shape applications in various fields such as aerospace, biomedical, and automotive, etc. The subject of this paper is the powder-based EBAM and will be referred simply as EBAM through the paper for the sake of space saving.

Despite of EBAM's capability and potential benefits, applications using such a technology are still not widespread. Part quality from EBAM is sensitive to the process parameters, and yet the setting from the manufacturer may not be necessarily optimal for different part geometries. Further, part quality variations have been a major factor that hinders the certification of EBAM parts for critical applications. Therefore, the effect of process parameters on part attributes need to be studied in order to efficiently implement EBAM applications. However, experimental testing is time consuming and costly. On the other hand, process physics modeling may offer a more efficient means to tackle such an issue. EBAM is a rather complicated process and fundamental understanding of process physics is also a key to improve the process performance and part quality. However, there is rather limited modeling work for EBAM reported in literature. Despite of increasing studies in the EBAM process, most have been for applications, case studies, or microstructures/properties, etc. Zäh and Lutzman developed a simplified heat transfer model of EBAM to study the scan speed and beam power effects on the weld-pool geometry [1]. Shen and Chou recently initiated a study to investigate the thermal phenomenon of the EBAM process. A finite element (FE) model incorporating Gaussian heat flux distribution, fusion latent heat, temperature-dependent thermal properties was developed to study the thermal response in the build volume when subject to a moving heat source of high intensity [2].

On the other hand, EBAM process measurements are important as well for model validations and process monitoring, but, fairly rare in literature. Zäh and Lutzman applied thermocouples, attached to the build plate, to evaluate temperature response during the EBAM process to evaluate the model developed by this research group [1]. However, because of very high temperatures and steep gradients, thermocouple techniques are limited in accuracy and resolutions. As EBAM, most AM technologies are thermally dominant processes and temperature distributions and history are critical to the process characteristics and performance. There have been different approaches attempted for temperature measurements in AM processes. Most studies used an infrared thermal camera to acquire temperature data, while a few studies used thermocouples to measure point temperatures. Some of the infrared cameras used included a Raytheon radiance HS infrared camera [3, 4], a Thermaviz two-wavelength pyrometer [5], and a FLIR Systems Prism DS digital infrared camera [6]. A Mikron M67S infrared temperature sensor [7] and a Raytech MR1S dual wavelength instrument [8] were also used to measure the average temperature at the center of the molten pool. Most of the cameras had a spectral band pass filter between 3 and 5 μm, although a longer range of 8 to 12 μm [9] and a short wavelength of 0.7 to 1.06 μm [10, 11] were also used. The frame rates used ranged from 1 frame every 2 seconds [5] to 300 frames per second [10]. The cameras were either mounted exterior to the process equipment or had a fiber optic cable mounted coaxially on a head inside a machine. A majority of the thermal cameras were calibrated using an ultrahigh temperature blackbody calibrator and a thermocouple. One camera was calibrated using a NIST tungsten filament [5]. An experimental apparatus used a high shutter-speed camera and a 337 nm near ultraviolet (UV) laser in conjunction with the infrared camera [10, 11]. Griffith et al. [6] used a 12-bit digital camera with a telephoto lens and a 650 nm broad band filter to capture images of a melt pool. According to the temperatures recorded with this method, the results were similar to thermocouple and infrared measurements except for those inside the melt region of the melt pool.

For thermocouple applications, Yang et al. [12] sandwiched a K-type thermocouple between metal tapes to record temperatures in an ultrasonic consolidation process. Sun et al. [13] and Pasandideh-Fard et al. [14] both embedded K-type thermocouples into the material deposition base of studied AM processes. Sun et al. studied the thermal cycles a part goes through during a fused deposition modeling process. On the other hand, Pasandideh-Fard et al. studied the solidification of tin droplets on a stainless steel plate. Both Yang et al. and Sun et al. used a sampling rate of 1000 Hz [12,13]. Besides, Griffith et al. [6] inserted C-type thermocouples into a build part during a laser engineered net shaping (LENS) process in order to study the severity of the thermal cycles caused by the process.

Measuring temperature has always been an interesting subject in most manufacturing process studies as it provides valuable insight of process details. However, temperature measurements can be difficult for different reasons, e.g., temperature range, material issues, and transient response, etc. It is especially challenging in some high powder, localized and high rate processes such as EBAM. For high temperature processes, non-contact measurements such as infrared are preferred. However, because of x-ray generations in EBAM processing, a leaded glass is attached on the viewport of the machine, and the glass may affect the transmission, In general, the transmission rate of a leaded glass for the infrared bandwidth can be very low, < 60% [15]. On the other hand, for the wavelength from 500 nm to 2 μm, the transmission rate of most glasses (transparent objects) is less sensitive. Hence, near-infrared (NIR) thermal cameras may be more suitable for such a task. Indeed, NIR thermal cameras have been employed for temperature measurement studies in different manufacturing processes.

Haferkamp et al. [16] used a CCD camera with a spectral range up to 1.3 μm to measure the temperature of cast aluminum alloy parts during solidification. A mold made of IR-transparent silica aerogel was used in order to capture NIR images of the cast part while it was in the mold. Ageorges et al. [17] used a Photometrics Sensys CCD Camera to measure the temperatures of the heating element during a resistance welding process. The camera detected wavelengths up to 0.9 μm. Temperatures from 180 °C to around 500 °C were in the measuring range of the camera. Outeiro et al. [18] also used a CCD camera to study the temperatures of the tool in a 3D cutting process. The camera used an 850 nm high pass filter. The temperature range of the camera was dependent on the length of the exposition time of the camera. The camera's minimum temperature ranged from 420 to 542 °C and its maximum temperature ranged from 549 to 757 °C.

M'Saoubi et al. [19] used a CCD senor based NIR imager with a spectral range of 0.85 to 1.1 μm to measure the tool temperature during a turning process. They compared the tool temperatures for various coatings, feed rates, and cutting speeds. In a continued study, the same research group [20] used the same NIR imager to measure the tool temperature during an orthogonal cutting process. The workpieces were made of carbon steel AISI 3115 and stainless steel AISI 316L. The effects that various heat treatments on the workpiece have on the tool temperatures were analyzed using the NIR images. Rech [21] conducted a similar experiment where the author used a CCD infrared camera to measure the tool temperature during a turning operation. The workpiece material was AISI 4142H steel. The experiment examined the tool coating effects on the tool temperatures. The camera had a detectable range of 500 to 1000 °C. The maximum temperature measured on the tool was 653 °C. Jackson and Gossard [22] used a

Canon 350D to measure the substrate temperature in a molecular beam epitaxy system. The spectral range of the camera was 720 to 1100 nm and the camera was able to measure the substrate temperatures in the range of 500 °C to 515 °C. Craeghs et al. [23] examined the effects of various factors during a laser melting process using a high speed NIR camera and a photodiode sensor to determine the temperatures of the melt pool. A 700 to 950 nm low pass filter was used for the camera. Mirrors were used to reflect the image of the process to the camera. The NIR images were analyzed to detect the edge of the melt pool by determining which isotherm corresponded with the edge.

In this research, an NIR thermal camera was tested to attempt temperature measurements in the EBAM process. The objective of the current phase was to evaluate the feasibility and capability of an NIR thermal camera for investigating the thermal characteristics of the EBAM process. The overall goal of this research is to achieve temperature measurements in the EBAM for process model validations and process monitoring, also to investigate process parameter effects on the thermal characteristics of the EBAM process.

Experimental Setup

The EBAM machine used for temperature measurements was an S12 system, from Arcam, at NASA's Marshall Space Flight Center (MSFC). Further, it was decided to acquire data images through the 127 mm diameter viewport at the front side of the machine, Figure 1. In addition to the leaded glass mentioned above, there is also a high-strength vacuum glass attached to the viewport, which will affect the radiation transmission as well at certain wavelengths. Thus, an NIR thermal camera, MCS640 from LumaSense, was used. The camera has a spectral range of 780 nm to 1080 nm wavelength, has a 640 by 480 uncooled focal plane array (FPA) sensor (amorphous Si based). The detectable temperature range is from 600 °C up to 3000 °C, with different ranges of calibrations. The maximum frame rate of the image capturing system is at 60 Hz. The general specification of the camera is listed in Table 1 below.

Table 1. Specification of the NIR thermal camera used.

Wavelength (nm)	FPA	Max frame rate (Hz)	Temperature range (°C)
780 – 1080	640 by 480	60	600 - 3000

Two types of lenses, with different focal distances, were employed for different purposes. One lens (A) has a minimal 500 mm working distance and a view area of 31 mm by 23 mm at 500 mm distance (FOV angle: 3.5° by 2.6°). The other one (B), a closed-up lens, has a nominal 350 mm working distance and with a view area of only 5.3 mm by 4.0 mm (FOV angle: 0.88° by 0.65°). Lens A results in a spatial resolution about 48 μm in both horizontal and vertical directions at 500 mm distance. On the other hand, Lens B gives a finer spatial resolution, approximately 8.3 μm. The thermal camera was calibrated in 3 different temperature ranges, for Lens A: (650 - 900, 850 - 1250, 1100 - 1800 °C), and for Lens B: (750 - 1100, 915 - 1400, 1320 - 2300 °C) using a black body. For Lens B, the calibration was conducted with and without glasses (identical to those used in S12) to estimate the overall transmission rate of the applied glasses. The transmission rate has been determined to be about 0.54. Emissivity was not known when the testing was conducted. Therefore, a value of 0.3 (for metal) was assumed; however,

this could probably be deviated from the actual values because of the powder material used and the high temperature condition involved. Further, the integration time for imaging is 16.25 ms, 1.7 ms, 50 µs for the temperature range 1 (low), 2 (medium) and 3 (high), respectively. The data acquisition system included a network cable and a laptop, connected via a gigabit Ethernet express card.

The S12 machine, thermal camera setup using a sturdy tripod, and the heat shield covering the build area are shown in Figure 1. Note that the heat shield that covers the build area has the slit area, where the view is made possible. The camera lens was set close to the glass window, straight targeting the build plate area. Figure 2 is a sketch showing the position and orientation of the camera, relative to the machine. The estimated vertical tilt angle was to be about 55°, no horizontal yaw or roll angle.

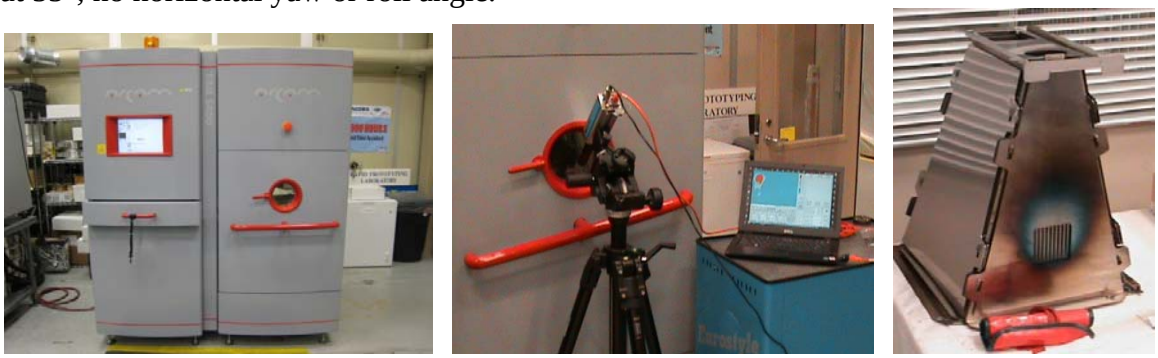

Figure 1. Left: EBAM machine, Center: thermal camera setup, and Right: heat shield.

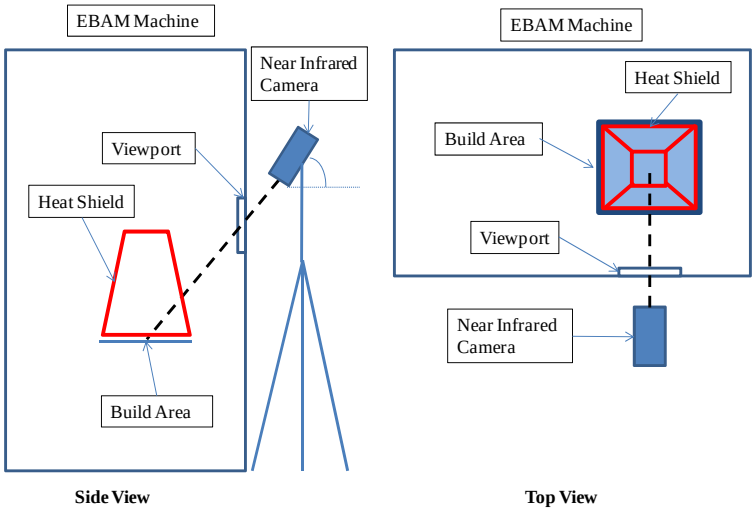

Figure 2. A sketch showing position and orientation of the camera relative to the EBAM machine (drawing not to scale).

The CAD model designed and built in the machine for temperature measurements using the Lens A was just a simple 25.4 mm square block. While the CAD model built for measurements using the Lens B was several thin-walled structures, shown in Figure 3. The length and width of each thin wall is 25.4 mm and 3.8 mm, respectively. The overall height of the model was 25.4 mm as well. The model was designed to evaluate the spatial resolution against the specification. The EBAM process parameters used including the beam voltage, offset

current, beam speed, etc., were default values typically employed for Ti-6Al-4V powders under normal geometry and operations.

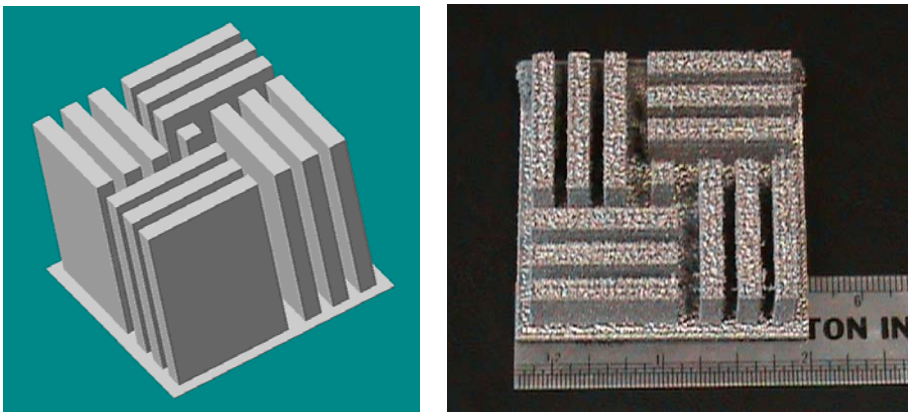

Figure 3. Build part in EBAM when measuring temperatures using Lens B.

Results and Discussion

The heating cycles in the EBAM process have several phases including build platform (start-plate) heating, preheating, contour melting and hatch melting, etc., and in each phase, some process parameters may be very different. First, once the required vacuum level is achieved, heating of the build platform (~10 mm thick stainless steel plate) is initiated, using a single beam scanning at a very high speed. The default target temperature level is around 730 °C (measured by a thermocouple attached to the bottom of the plate). During this phase, the NIR thermal camera was not able to detect temperature rise until a later stage. It was also noted that the heating is paused at about 400 to 450 °C (plate bottom temperature) for about 10 to 20 minutes for heat shield out-gassing.

A few sections below describe the build process and thermal images acquired when using Lens A, in making the 25.4 mm square block in the EBAM machine. The build cycle starts when the start-plate bottom temperature reaches 730 °C. During each cycle (each layer fabrication), the process involves powder spreading (via a raking mechanism), powder preheating, contour melting, and hatch melting. During the powder spread, a metal rake is applied to distribute one layer of powders, 100 μm in this test. The build part surface temperature is instantaneously reduced, to a level below what the thermal camera can sense, since the powders spread from the hopper have a much lower temperature.

In the next phase, powder preheating cycle starts using also a single beam at a high speed (visually showing multiple scanning line pattern), and involves multiple scanning passes (alternative raster pattern at different layers) to reach a uniform high temperature across the entire powder bed surface. Row 1 of Figure 4 shows examples of NIR thermal images during preheating at Low and Medium Temperature Ranges, respectively. The line pattern of high temperature zones is noticed, as high as over 1000 °C. Another observation to point out is that, recalling the camera has to see through the slit area of the heat shield (Figure 1, Right photo), the seemingly vertical bands observed from the Low Temperature Range represent the areas blocked by the uncut portion of the heat shield.

Following the preheating, the contour melting takes place, during which multiple split beams move across the powder-layer surface tracing the boundary defined by the cross-section at that specific layer (a square in this case) of the build model. It was observed that there appears to have 2 stages in this phase. During the first stage, several split electron beams quickly pulse statically around the part boundary of that layer, starting to melt and fuse the powders together. Figure 4, Row 2 images show examples of NIR images occurred in the first part of contour melting collected at 3 Temperature Ranges. The boundary of the model at that specific layer can be clearly observed, evidenced by the high temperature spots. The distance (in pixel number) between the left and right borders was used to calculate the corresponding spatial resolution, estimated to be 47.6 μm, consistent to the spec. Note that due to the vertical tilt angle of the camera setting, the dimension along the vertical direction is slightly distorted. During the second stage of the contour melting, several electron beams (split) outline the outer boundary more slowly, causing completely melting of the contour. Figure 4, Row 3 images show examples of NIR images occurred in the second stage of contour melting, also at 3 Temperature Ranges.

The final phase of each layer build cycle is the hatch melting, during which a single beam scans through the inside of the contour, with a straight rater pattern. The scanning speed is lower than those used during the preheating and contour melting, though visually still quite fast. Figure 5 shows examples of NIR images acquired during the hatch melting, again with 3 Temperature Ranges. It is recognized that the thermal behavior in the hatch melting resembles the features of common moving heat source applications, a localized high temperature zone followed by a tail with rapid temperature decay, opposite to the moving direction. The temperature range is very high, with the peak well above the melting point of Ti-6Al-4V, 1650 °C.

The thermal images observations during the build using Lens B, same setup as using Lens A except a shorter distance to the target, were quite similar to those in the square-block build with Lens A. They followed the various heating phases described earlier, however, with a smaller view area. Since the purpose of this particular testing was to evaluate the spatial resolution of the thermal camera and lens, this section just describes the contour melting stage, during which the spatial resolution was determined. Figure 6 shows the NIR image example during contour melting (first stage) in the area including one of the thin wall columns, horizontal orientation. The vertical distance between the high-temperature zones (centers) was used to estimate the spatial resolution, estimated to be about 16 μm. Due to the vertical tilt angle, note that the resolution is distorted. On the other hand, the images taken during contour melting of the vertical thin-wall sections gave a spatial resolution of 12 μm. Another observation is that because of a much smaller area in the scanned cross-section, the hatch melting does not clearly show the moving heat source phenomenon illustrated in previous sections. The fast scanning combined with the short transverse distance to travel results in such a result.

The acquired thermal images/videos offer visualization to interpret the EBAM process. In addition, the data collected can be analyzed to obtain more insight of the process phenomena. Two examples are discussed below. Figure 7 below shows an example of the melt-pool shape and size during the hatch melting (square block building). The melt pool has a long axis of 1.81 mm and a short axis of 0.67 mm.

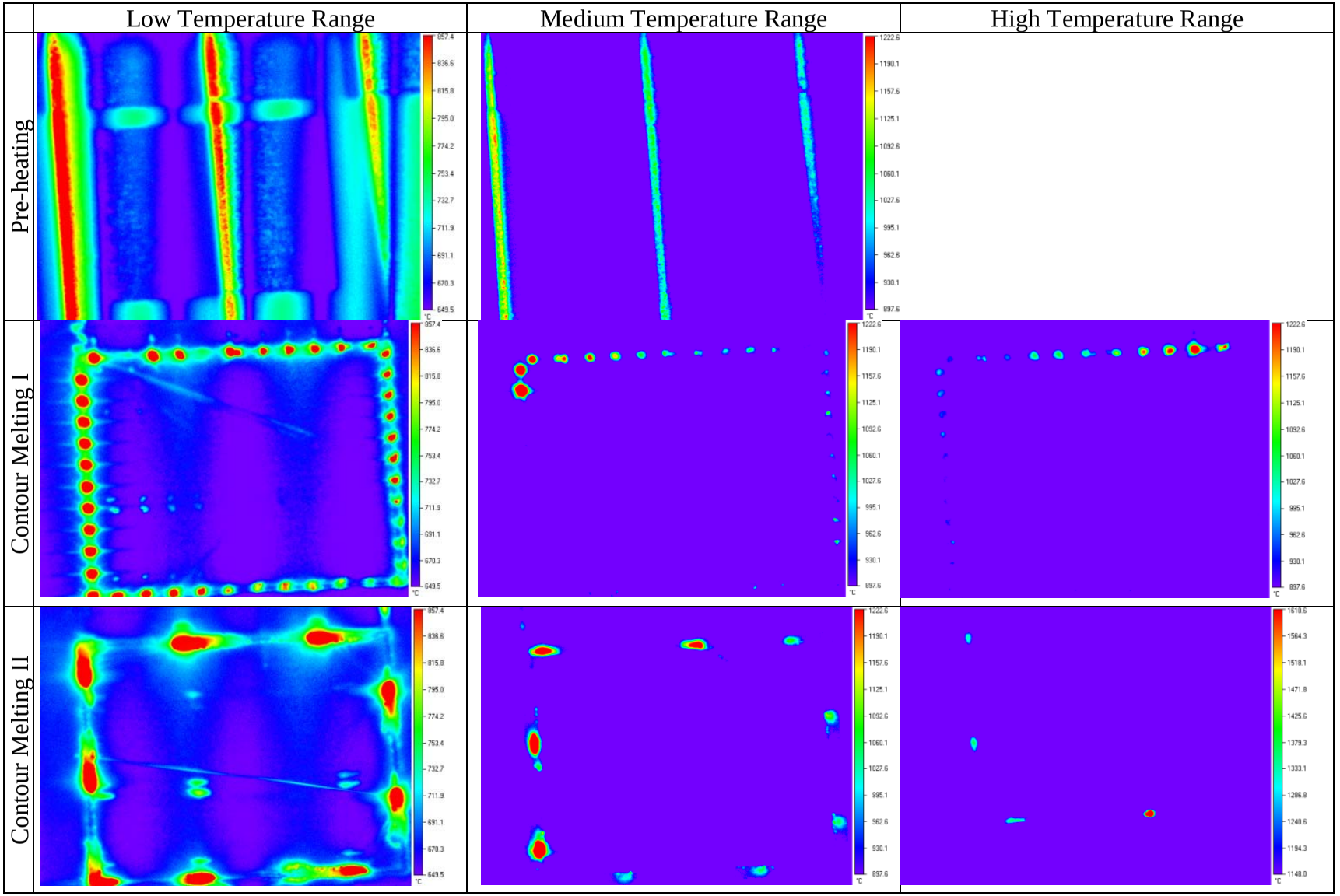

Figure 4. NIR images at different phases and different temperature ranges.

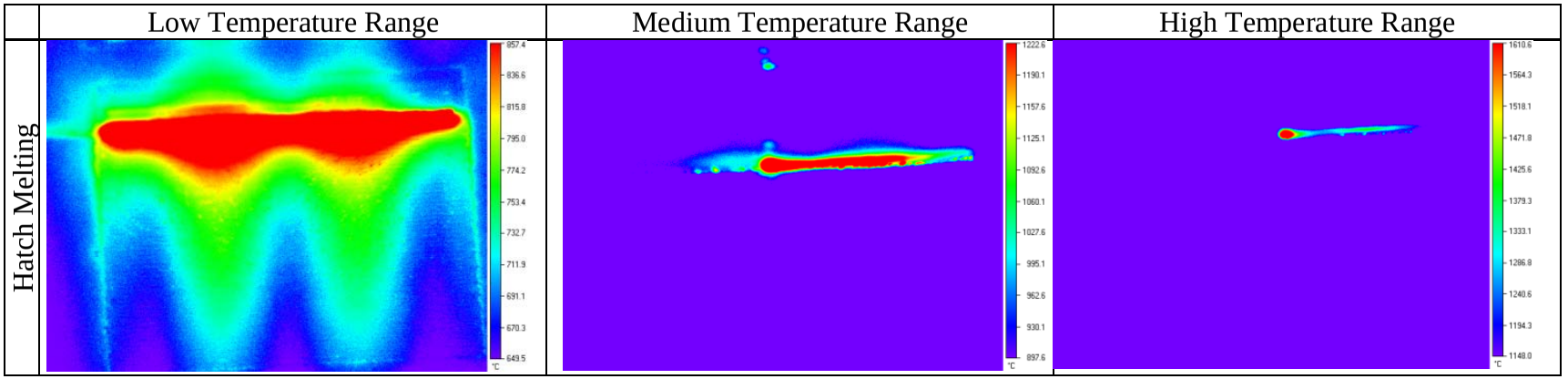

Figure 5. NIR images during hatch melting.

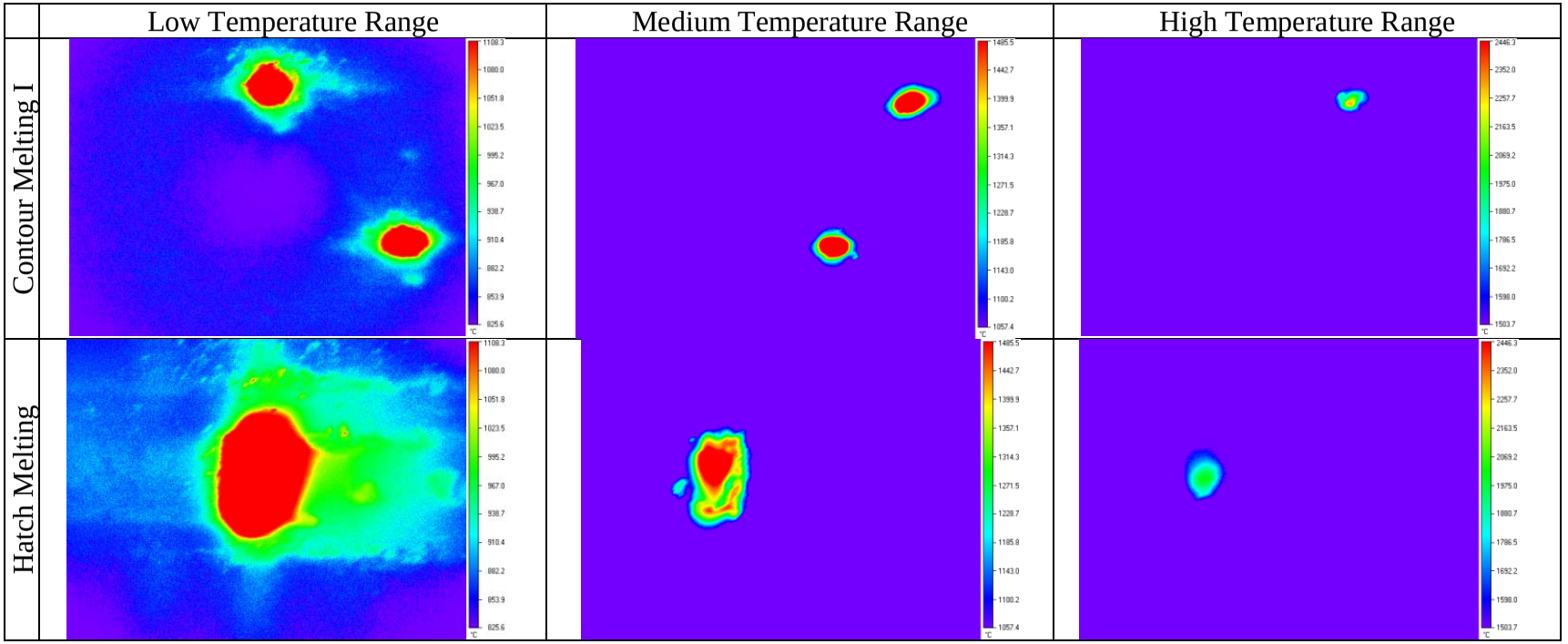

Figure 6. NIR images collected during fabricating a multiple thin-wall part.

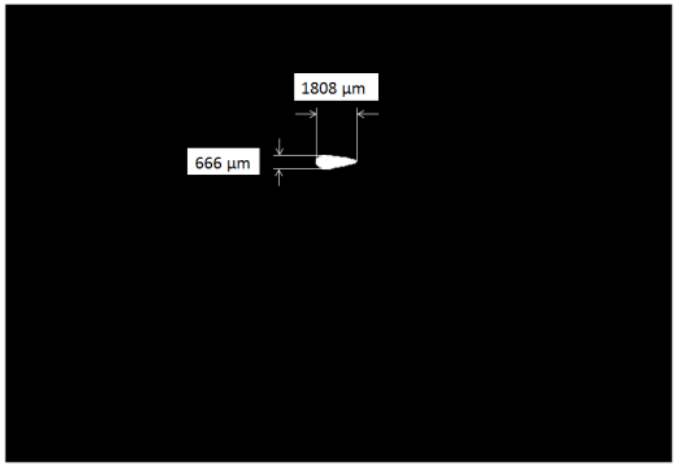

Figure 7. An example of the melt pool shape and size.

Figure 8 below shows an example of a temperature profile across the melt pool center, along the electron beam moving direction during the hatch melting, at High Temperature Range. Data from multiple frames, i.e., electron beams at different locations and different files was analyzed. Both of the average (blue line) and standard deviation (vertical bars) values are shown. The result shows good repeatability of the temperature distributions along the beam moving direction. Again, the profile exhibits the thermal behavior similar to a moving source of heat phenomenon: rapid temperature rise at the heat source front, and a quick decay in the back. Further, the phase change region can also be clearly identified as the plateau at around 1450 C, which should correspond to the melting point of Ti-6Al-4V. Note that, as explained earlier, the emissivity of Ti powders and the NIR transmission ratio of the glasses were both assumed (Lens A), mostly inaccurate, during this experiment. The temperature profile may offer some hints for the emissivity estimate.

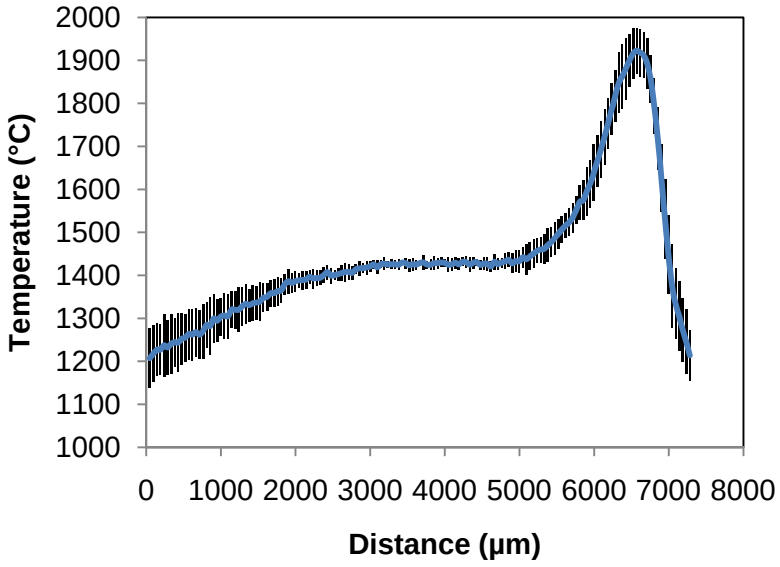

Figure 8. Temperature profile across the melt pool, along the electron beam moving direction (Average data with standard deviation bars).

Conclusions

Temperature measurements during the EBAM process have been attempted using an NIR thermal camera incorporating 2 different lenses individually. Two different CAD models were fabricated separately for acquiring thermal images during the build in the EBAM machine. The feasibility and capability have been evaluated. The major results are summarized as below.

- Temperature measurements in the EBAM process by an NIR thermal camera are feasible; the camera is able to capture different events at different temperature ranges.
- Spatial resolutions, lens dependent, were confirmed by images collected during the build of particularly designed models, about 12 μm when using a closed-up lens.
- The temperature measurements in the hatch melting are repeatable, as evidenced in Figure 8.
- One of the challenges is to determine the emissivity of Ti powders at high temperatures.
- Future work will include comparison with the simulations for model validations and studying process parameter effects on the thermal characteristics in the EBAM process.

Acknowledgement

This research is supported by NASA, No. NNX11AM11A, and is a collaboration between The University of Alabama and MSFC. Support from Majid Babai, Chief of Nonmetallic Branch at MSFC, is greatly appreciated.

References

[1] Zäh M. F. and Lutzmann S., (2010), "Modelling and simulation of electron beam melting," Production Engineering, 4(1), pp. 15-23.

[2] Shen, N. and K. Chou, (2012), "Thermal Modeling of Electron Beam Additive Manufacturing Process – Powder Sintering Effect," ASME International Manufacturing Science and Engineering Conference, Notre Dame, IN, June 4-8, 2012 (MSEC2012-7253).

[3] Fischer, P., Locher, M., Romano, V., Weber, H. P., Kolossov, S., Glardon, R., 2004, "Temperature measurements during selective laser sintering of titanium powder," International Journal of Machine Tools and Manufacture, 44, pp. 1293-1296.

[4] Kolossov, S., Boillat, E., Glardon, R., Fischer, P., Locher, M., 2004, "3D FE simulation for temperature evolution in the selective laser sintering process," International Journal of Machine Tools and Manufacture, 44, pp. 117-123.

[5] Wang, L., Felicelli, S. D., Craig, J. D., 2009, "Experimental and numerical study of the LENS rapid fabrication process," Journal of Manufacturing Science and Engineering, 131, pp. 1-8.

[6] Griffith, M. L., Schlienger, M. E., Harwell, L. D., Oliver, M. S., Baldwin, M. D., Entz, M. T., Essien, M., Brooks, J., Robino, C. V., Smugeresky, J. E., Hofmeister, W. H., Wert, M. J., Nelson, D. V., 1999, "Understanding thermal behavior in the LENS process," Materials and Design, 20, pp. 107-113.

[7] Ho, H. C. H., Cheung, W. L., Gibson, I., 2002, "Effects of graphite powder on the laser sintering behavior of polycarbonate," Rapid Prototyping Journal, 8, 233-242.

[8] Gao, Y., Xing, J., Zhang, J., Luo, N., Zheng, H., 2008, "Research on the measurement method of selective laser sintering (SLS) transient temperature," Optik – International Journal for Light and Electron Optics, 119, pp. 618-623.

[9] Doumanidis, C., Kwak, Y. M., 2001, "Geometry Modeling and Control by Infrared and Laser Sensing in Thermal Manufacturing with Material Deposition," Journal of Manufacturing Science Engineering, 123, pp. 45-53.

[10] Hu, D., Kovaceic, R., 2003, "Modeling and measuring the thermal behavior of the molten pool in closed loop controlled laser-based additive manufacturing," Proceedings of the Institution of Mechanical Engineers, Part B: Journal of Engineering Manufacture, 217, pp. 441-452.

[11] Hu, D., Kovaceic, R., 2003, "Sensing, modeling and control for laser based additive manufacturing," International Journal of Machine Tools and Manufacture, 43, pp. 51-60.

[12] Yang, Y., Janaki Ram, G. D., Stucker, B. E., 2009, "Bond formation and fiber embedment during ultrasonic consolidation," Journal of Materials Processing Technology, 209, pp. 4915-4924.

[13] Sun, Q., Rizvi, G. M., Bellehumeur, C. T., Gu, P., 2008, "Effect of processing conditions on the bonding quality of FDM," Rapid Prototyping Journal, 14, pp. 72-80.

[14] Pasandideh-Fard, M., Bohla, R., Chandra, S., Mostaghimi, J., 1998, "Deposition of tin droplets on a steel plate: simulations and experiments," International Journal of Heat and Mass Transfer, 41, pp. 2929-2945.

[15] The Infrared Handbook Prepared by: The Infrared Information Analysis (IRIA) Center, Environmental Research Institute of Michigan for the Office of Naval Research, Dept. of Navy, Washington, DC. 3rd edition: 1989 Editors: William L. Wolfe and George J Zissis Library of Congress Catalog Card No.: 77-90786.

[16] Haferkamp, H., Back, F. W., Niemeyer, M., Viets, R., Weber, J., Breuer, M., Krüssel, T., 1999, "Tracing Thermal Process of Permanent Mould Casting," 1999 IEEE International Symposium on Industrial Electronics, 3, pp. 1442-1447.

[17] Ageorges, C., Ye, L., Hou, M., 2000, "Experimental investigation of the resistance welding for thermoplastic-matrix composites. Part I: heating element and heat transfer," Composites Science and Technology, 60, pp. 1027-1039.

[18] Outeiro, J. C., Dias, A. M., Lebrun, J. L., 2004, "Experimental Assessment of Temperature Distribution in Three-Dimensional Cutting Process," Machining Science and Technology, 8, pp. 357-376.

[19] M'Saoubi, R., Chandrasekaran, H., 2004, "Investigation of the effects of tool micro-geometry and coating on tool temperature during orthogonal turning of quenched and tempered steel," International Journal of Machine Tools & Manufacture, 44, pp. 213-234.

[20] M'Saubi, R., Chandrasekaran, H., 2011, "Experimental study and modeling of tool temperature distribution in orthogonal cutting of AISI 316L and AISI 3115 steels," International Journal of Advanced Manufacturing Technology, 56, pp. 865-877.

[21] Rech, J., 2006, “Influence of cutting tool coatings on the tribological phenomena at the tool-chip interface in orthogonal dry turning,” Surface & Coatings Technology, 200, pp. 5132-5139.

[22] Jackson, A. W., Gossard, A. C., 2007, “Thermal imaging of wafer temperature in MBE using a digital camera,” Journal of Crystal Growth, 301-302, pp. 105-108.

[23] Craeghs, T., Clijsters, S., Yasa, E., Bechmann, F., Berumen, S., Kruth, J. P., 2011, “Determination of geometrical factors in Layerwise Laser Melting using optical process monitoring,” Optics and Lasers in Engineering, 49, pp. 1440-1446.